

InAs light-to-heavy hole effective mass ratio determined experimentally from mobility spectrum analysis

Jarosław Wróbel^{1*}, Gilberto A. Umana-Membreno², Jacek Boguski¹, Sebastian Złotnik¹, Andrzej Kowalewski¹, Paweł Moszczyński³, Jarek Antoszewski², Lorenzo Faraone², Jerzy Wróbel^{1,4}

¹Institute of Applied Physics, Military University of Technology, gen. Sylwestra Kaliskiego 2, 00-908 Warsaw, Poland

²Dept. of Electrical, Electronic and Computer Engineering, The University of Western Australia, 35 Stirling Highway, Crawley WA 6009, Australia

³Faculty of Cybernetics, Military University of Technology, gen. Sylwestra Kaliskiego 2, 00-908 Warsaw, Poland

⁴Institute of Physics, Polish Academy of Sciences, Aleja Lotników 32/46, 02-668 Warsaw, Poland

Article info

Article history:

Received 22 Oct. 2022

Received in revised form 05 Dec. 2022

Accepted 23 Dec. 2022

Available on-line 24 Feb. 2023

Keywords:

Indium arsenide; effective masses; energy band warping; magnetotransport; mobility spectrum analysis.

Abstract

Careful selection of the physical model of the material for a specific doping and selected operating temperatures is a non-trivial task. In numerical simulations that optimize practical devices such as detectors or lasers architecture, this challenge can be very difficult. However, even for such a well-known material as a 5 μm thick layer of indium arsenide on a semi-insulating gallium arsenide substrate, choosing a realistic set of band structure parameters for valence bands is remarkable. Here, the authors test the applicability range of various models of the valence band geometry, using a series of InAs samples with varying levels of p-type doping. Carefully prepared and pretested the van der Pauw geometry samples have been used for magneto-transport data acquisition in the 20–300 K temperature range and magnetic fields up to ± 15 T, combined with a mobility spectra analysis. It was shown that in a degenerate statistic regime, temperature trends of mobility for heavy- and light-holes are uncorrelated. It has also been shown that parameters of the valence band effective masses with warping effect inclusion should be used for selected acceptor dopant levels and range of temperatures.

1. Introduction

A^{III}-B^V semiconductor compounds, especially 6.1 Å family materials, play an important role as light emitters and absorbers over the infrared (IR) range [1]. Alloys like InAs_{1-x}Sb_x due to their bandgap flexibility [2] are often used as an active region in quantum wells [3], superlattices [4], or other low dimensional structures [5]. Moreover, it exhibits very high electron mobilities [6], with better thermal stability and lower technology price than mercury/cadmium/telluride (MCT) equivalent materials for infrared devices [7]. InAs as a special case of InAs_{1-x}Sb_x alloy seems to be particularly important. A better understanding of its basic physical properties is currently the subject of intensified research [8, 9]. In this context, a fundamental role is played by a deep understanding of the

InAs structure of energy bands, especially for valence bands.

The motivation for this work was very large literature discrepancies in estimating the density-of-states (DOS) effective mass for the light-holes (m_{lh}^{dos}). The selective review performed by the authors indicated that only two experimental papers conducted in 1960s for cryogenic temperatures are available on this topic [10, 11]. For all other papers, the discrepancies in m_{lh}^{dos} values exceed 100% [10–25].

Now, with the greater availability of high-field superconducting electromagnets [26] and advanced data processing tools [27], there are opportunities to analyse multi-channel charge carrier transport [28]. In this paper, they allowed the authors to draw conclusions about the energy band parameters of light-holes, which account for about 1 in 1000 other charge carriers involved in the conductivity.

*Corresponding author at: jaroslaw.wrobel@wat.edu.pl

2. Materials and methods

2.1. Series of indium arsenide growths and sample preparation

The series of five InAs layers have been grown on (001)-oriented semi-insulating epi-ready 2-in GaAs substrates with 2° offcut towards <110> in a RIBER Compact 21-DZ solid-source molecular beam epitaxy (MBE) system [29]. After thermal desorption of oxides, a 250 nm thick non-intentionally doped (n.i.d.) GaAs layers were deposited to smooth the surface and to cap a residual contamination. After this stage, Be-doped InAs epilayers were deposited with a concentration of beryllium changing every half order of magnitude. Basic parameters of these layers have been gathered in Table 1.

Table 1.
Basic parameters of the considered InAs layers.

Wafer index (-)	Thickness (μm)	Be doping [p-type] (cm^{-3})
#1	4.55	$5 \cdot 10^{18}$
#2	4.55	$1 \cdot 10^{18}$
#3	4.58	$5 \cdot 10^{17}$
#4	4.57	$1 \cdot 10^{17}$
#5	4.30	$5 \cdot 10^{16}$

Next, the van der Pauw circular-shape structures were fully processed by including positive photolithography and wet etching down to GaAs substrate in a mixture of orthophosphoric acid, citric acid, hydrogen peroxide, and water solution [30]. Metallization for assuring electrical, ohmic contact was made by electroplating of gold which has worked perfectly for this class of materials in the authors' previous experiments [31]. Here, no passivation was used so as not to disturb the native electron transport information. At the final stage of the processing, selected $4 \times 4 \text{ mm}^2$ specimen areas were precisely cut by a diamond scribe and mounted to sample holders. Each metallization area was semi-automatically bonded with a gold wire of a diameter of 25 μm .

2.2. Hall effect measurements

The magneto-transport characterisation was performed using a superconducting 16T Cryogen-Free Magnet System (CFMS16T) made by Cryogenic Ltd. Each of the samples was placed in the centre of a solenoid, where the magnetic induction (B) homogeneity is better than $\leq 0.1\%$ total variation over a 10 mm diameter sphere. In this part of the magnet, the variable temperature insert was set to temperatures (T) ranging from 20 to 300 K in steps of 20 K. Even though the samples were in the direct windage of the 5.2 He purge, the conditions were quasi-static in the heat transfer sense. In the worst case, at room temperature, the temperature stabilisation (standard deviation from mean) was better than 50 mK, monitored by the Cernox™ sensor.

Before performing the actual data acquisition, all samples were subjected to preliminary contact linearity tests by method presented earlier [32]. All of them passed these tests in the entire considered temperature range. An

Agilent B2902A source measure unit, a two-channel programmable multi-meter, was used to perform this test.

Target Hall data acquisition has been completed in a constant voltage bias during $\pm 15 \text{ T}$ B -field sweeps in the step mode. A Keithley 2400 source meter and a Keithley 2182A nanovoltmeter were used for this purpose. For each sweep in B -field at constant temperature, 60 sets of van der Pauw data uniformly distributed on a \log_{10} scale were collected.

2.3. Mobility spectrum analysis

For the main goal of this paper, namely, obtaining the m_{lh}^{dos} -to- m_{hh}^{dos} ratio value, the general form of the formula for hole concentration (n_h) has been used

$$n_h = \left[\frac{2\pi m_h^{dos} k_B T}{h^2} \right]^{3/2} \exp \left[\frac{E_v - E_F}{k_B T} \right], \quad (1)$$

where h is the Planck constant, k_B is the Boltzmann constant, E_v is the valence band extremum, E_F is the Fermi level, m_h^{dos} is the DOS effective mass. Defining the two separate concentrations by the use of (1): n_{lh} and n_{hh} for light-hole and heavy-hole band, respectively, the m_{lh}^{dos} -to- m_{hh}^{dos} ratio takes the form [33]

$$\frac{n_{hh}}{n_{lh}} = \left[\frac{m_{hh}^{dos}}{m_{lh}^{dos}} \right]^{3/2}. \quad (2)$$

This relation is useful only when precise measurements of separated hole concentrations are possible. The mobility spectrum analysis (MSA) [27] was used to achieve this goal. The basics of such method is to analyse the magnetic field induction (B) dependence of the conductivity tensor components $\sigma_{xx}(B)$ and $\sigma_{xy}(B)$, which are calculated from the experimental values of the Hall constant $R_H(B)$ and the sheet resistance $R_s(B)$:

$$\sigma_{xx}(B) = \frac{R_s(B)}{R_s^2(B) + R_H^2(B)B^2} \quad (3a)$$

$$\sigma_{xy}(B) = \frac{R_H(B)B}{R_s^2(B) + R_H^2(B)B^2}. \quad (3b)$$

These relations contain information about all carrier species present in a characterised sample. The essence of the MSA method is to search for such a form of the mobility spectrum function $S(\mu) \geq 0$ which satisfies the following relations:

$$\sigma_{xx}(B) = \int_{-\infty}^{\infty} \frac{S(\mu)}{1 + \mu^2 B^2} d\mu \quad (4a)$$

$$\sigma_{xy}(B) = \int_{-\infty}^{\infty} \frac{S(\mu)\mu B}{1 + \mu^2 B^2} d\mu. \quad (4b)$$

Here, it is assumed that conductivity tensor components can be expressed as integrals of Drude-like terms, with $e n \mu$ and $e p \mu$ factors replaced by a continuous function of $S(\mu) d\mu$. The symbols p and n are the hole and electron sheet densities respectively, μ is the mobility, and e is the

electronic charge. Obtaining "correct" form of the function $S(\mu)d\mu$ is not a numerically easy task, but there are several different methods such as: QMSA [34], ME-MSA [35], or HR-MSA [36]. In this work, the authors used their own algorithm which will be described elsewhere.

3. Results and discussion

3.1. Mobility spectra for series of p-doped InAs samples

The parameters of narrow bandgap materials are usually strongly dependent on temperature. It is very difficult or even impossible to infer about electron transport parameters from single Hall temperature data without complex numerical modelling. Moreover, results for some temperatures may potentially lead to mistakes, for the samples whose levels of impurity concentrations are so high that the location of the Fermi level does not satisfy the assumption of the relationship $(E_v - E_F) > 3k_B T$. For this reason, the paper presents spectra for a wide range of temperatures to facilitate the final interpretations.

Figure 1 presents the mobility spectra for the highest p-type doped InAs sample (#1, $N_A = 5.0 \cdot 10^{18} \text{ cm}^{-3}$). Most of the carrier species have a positive sign of mobility, which means that they are hole-like particles. However, despite the very acceptor concentration, low density electron-like carriers were detectable. In the literature, the origin of the electrons in p-InAs is most often attributed to the accumulation layer at the surface [37, 38]. In this paper, however, the authors will concentrate on the hole-like particles, which will be discussed in detail for different doping levels.

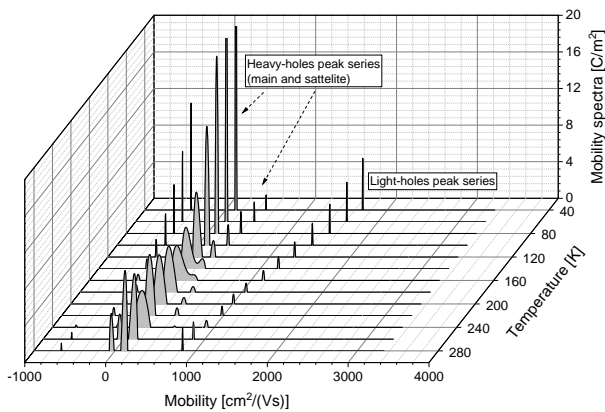


Fig. 1. The set of mobility spectra calculation results for the highest p-type doped sample (Sample #1, $N_A = 5 \cdot 10^{18} \text{ cm}^{-3}$).

For samples with $N_A > 1 \cdot 10^{18} \text{ cm}^{-3}$, the conductivity peaks with $\mu(T) = \langle 800, 1700 \rangle \text{ cm}^2/(\text{Vs})$ are attributed to light-holes [39], whereas the lower mobility peaks with $\mu(T) = \langle 80, 130 \rangle \text{ cm}^2/(\text{Vs})$ are attributed to heavy-holes. This carrier species assignment is consistent with the latter having the highest effective mass and highest carrier concentration, according to (1). Thus, the largest area under the selected peak is observed, which corresponds to the total heavy-hole concentration. The detailed definition of n_{hh} and n_{lh} will be given in section 3.2.

The most challenging for interpretation are narrow peaks with almost temperature-independent mobility

$\mu \approx 400 \text{ cm}^2/(\text{Vs})$. Their origin could be related to the hopping-like transport of carriers through the impurity band, which is normally formed for a high dopant level. However, relatively high mobilities and lack of clear temperature trend (Figs. 1–3) are not typical for hopping [40]. Therefore, the peaks are rather special “satellites” related to the heavy-hole band. The satellite for thin samples might be connected to the unrelaxed strain in thin epitaxial films [39], or with a thin interfacial layer between the GaAs buffer/p-InAs. However, in this case, layers are fully relaxed with almost 5 μm thickness. The authors suggest that observed satellites occur as a consequence of a highly anisotropic band structure [41]. The very high anisotropy of heavy-holes in indium arsenide [42] is sometimes referred to as “band warping” effect [43–45].

For the results presented in Fig. 2, corresponding to sample 2, only hole-like carrier species were predominately observed at higher mobility values, as expected for lower Be-doping level. The mobilities of the conductivity peaks attributed to light-holes increased to $\mu(T) = \langle 1100, 3100 \rangle \text{ cm}^2/(\text{Vs})$. The mobility of the dominant conductivity peak ascribed to heavy-holes doubled in magnitude, with a maximum mean mobility value of $\mu(T) = \langle 150, 300 \rangle \text{ cm}^2/(\text{Vs})$ at a near liquid nitrogen temperature (80 K). At the same temperature, the satellite peak vanishes which may indicate that Fermi level crosses the edge of valence band.

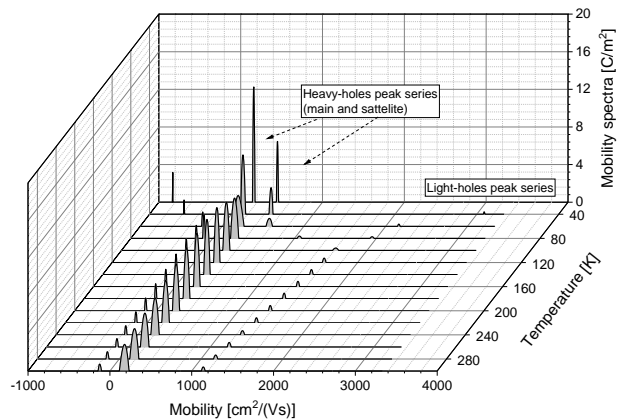


Fig. 2. The set of mobility spectra calculation results for the sample #2 ($N_A = 1 \cdot 10^{18} \text{ cm}^{-3}$).

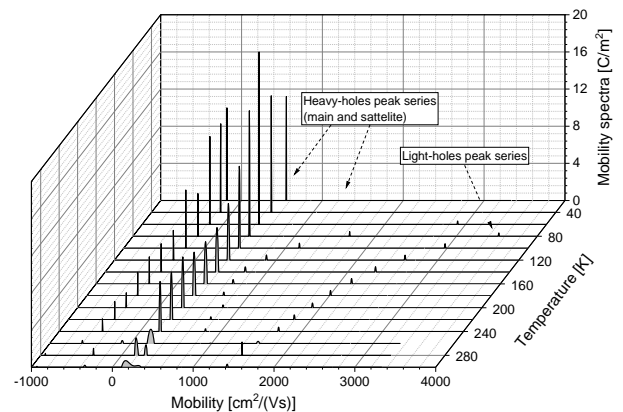


Fig. 3. The set of mobility spectra calculation results for the sample #3 ($N_A = 5 \cdot 10^{17} \text{ cm}^{-3}$).

Figure 3 shows data for a still lower doping level. The contribution of holes to the total conductivity decreased further and the role of surface transport via electron-like channels increased. Nevertheless, the scattering rate for holes also decreased and the mobilities of valence band carriers are higher, as compared to samples #1 and #2. In particular, the peaks attributed to the light-holes are observed for $\mu(T) = \langle 1400, 5100 \rangle \text{ cm}^2/(\text{Vs})$, reaching the maximum at temperature $T = 60 \text{ K}$. The mobility of heavy-holes is almost two times larger as compared to sample #2, the main spectral peak is now observed within the $\mu(T) = \langle 200, 450 \rangle \text{ cm}^2/(\text{Vs})$ range. Interestingly, the series of satellite peaks, detectable only at the lowest temperatures in other samples, were found to be present over almost at the entire temperature range, with mobilities $\mu(T) = \langle 600, 2900 \rangle \text{ cm}^2/(\text{Vs})$. Moreover, the satellite peaks move with temperature on the mobility axis almost parallel to the heavy-holes peak, down to $T = 120 \text{ K}$. It suggests that the presence of those additional spectral lines is indeed related to the significant “warping” of the heavy-hole band.

Further lowering of the concentration of acceptor impurities to $N_A = 1.0 \cdot 10^{17} \text{ cm}^{-3}$ and below (samples #4 and #5) leads to the increased role of electron-like surface channels, which are not discussed here. For the sample #4, the total electron conductivity becomes almost equal to the total hole conductivity. Such conditions are one of the most computationally difficult for MSA algorithms and carry a greater risk of non-physical numerical “artifacts” and errors in determined carrier densities. For this reason, the results of the calculations for sample #4 are not included in the graphs.

3.2. Temperature trends of heavy- and light-hole mobilities and concentrations

The temperature trends of heavy- and light-hole mobilities have been gathered in Figs. 4 and 5. Starting from sample #1 with the highest acceptor doping level, it can be observed that the mobility of light-holes for entire temperature range monotonically decreases according to the relation $\mu \sim T^{-\gamma}$ (red dots in Fig. 5). It is characteristic for a phonon scattering. Under the same conditions, a series of heavy-hole mobilities moves in a sideways trend, reaching the local minimums for 140 and 240 K. Both bands for this acceptor level are in the entire temperature range in degenerate regime (i.e., Fermi level lies inside the valence bands). However, only for this doping, the heavy- $\mu_{hh}(T)$ and light-holes $\mu_{lh}(T)$ trends show different behaviour pointing to various mechanisms dominating in carrier scattering for InAs:Be metallic phase.

This observation seems to be confirmed also in samples # 2 and # 3, at $T < 100 \text{ K}$. For these conditions, $\mu_{hh}(T)$ and $\mu_{lh}(T)$ trends are evidently uncorrelated and, what is very interesting, lowering the temperature (moving the Fermi level below valence band extremum) causes a rapid increase in the mobility of light holes.

On the other hand, for samples # 2 and # 3 over the range $T = \langle 100, 300 \rangle \text{ K}$, trends of $\mu_{hh}(T)$ and $\mu_{lh}(T)$ for the same samples are highly correlated differing only between the samples in the slope angle of the plots. Namely, for sample #3 (green plots), which has lower doping density than sample #2, the lower acceptor doping

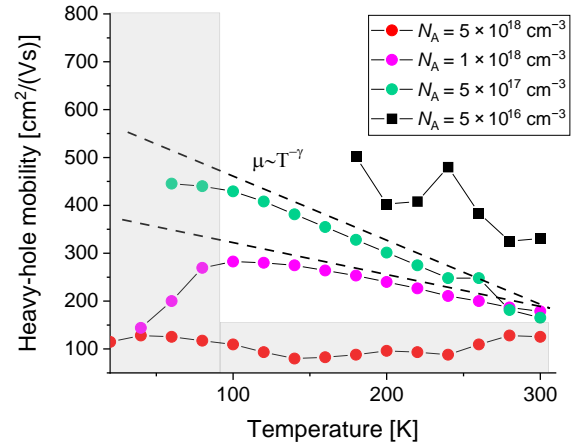


Fig. 4. The set of heavy-holes mean-mobility values vs. temperature for a series of InAs:Be samples. The shaded area is interpreted as being related to the degenerate regime.

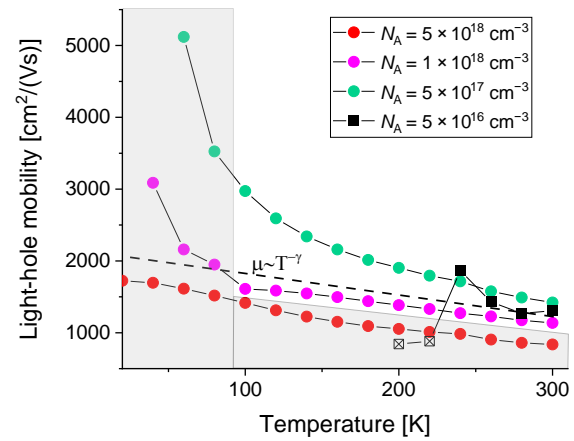


Fig. 5. The set of light-holes mean-mobility values vs. temperature for the series of InAs:Be samples. The shaded area is interpreted as being related to the degenerate regime.

level (purple plots) results in increasingly higher mobility values as temperature is lowered.

The last of the family of plots considered is related to sample #5. The relatively stable $\mu(T)$ results were obtained only for temperatures close to room temperature (black squares) and the authors considered the results for some individual points to be non-physical (crossed out squares). However, even for this sample with a strong dominance of surface conductivity channels, the trends seem to confirm previous observations.

For the MSA method, the hole concentrations are proportional to the integral under the part of $S^{lh}(\mu)$ and $S^{hh}(\mu)$ spectra (see Figs. 1–3) that are assigned to it

$$n_{lh} = \frac{1}{q} \int \frac{S^{lh}(\mu)}{\mu} d\mu \quad (5a)$$

$$n_{hh} = \frac{1}{q} \int \frac{S^{hh}(\mu)}{\mu} d\mu, \quad (5b)$$

with the proviso that for the n_{hh} integral, the integration takes place under both the plot of the main peak and the satellite. Based on (5a) and (5b), the temperature trends of heavy- and light-hole concentrations have been gathered in Figs. 6 and 7.

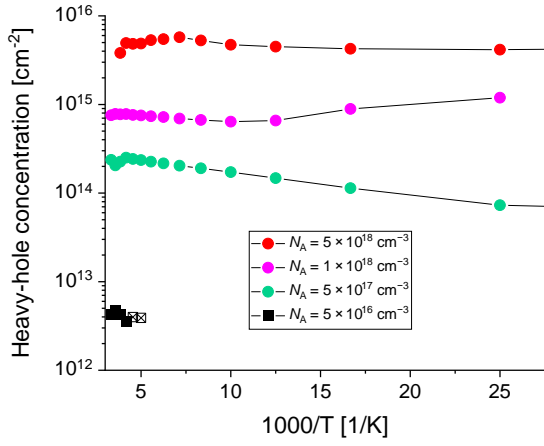


Fig. 6. The set of heavy-hole concentrations for the series of InAs:Be samples.

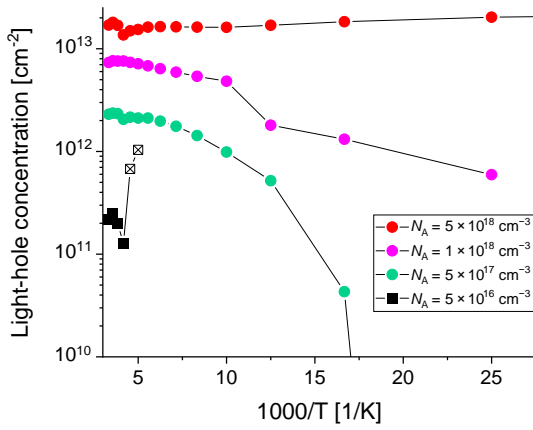


Fig. 7. The set of light-hole concentrations for the series of InAs:Be samples.

The symbols and colours of the data series remained the same as in Figs. 4 and 5. However, due to the analysis of concentrations as thermal processes, i.e., $n = n_0 \exp(-E_a/k_B T)$, where E_a is the activation energy, the graphs are presented on a 1000-on-T scale.

In such graphical representation, the flattening of the graph means $E_a \approx 0$ (because for every i -th point of N^i , the relation $n^i \approx n_0$ is satisfied). This is a typical situation for a metal and, in this case, it is characteristic of sample #1 for which both $n_{lh} = f(1000/T)$ and $n_{hh} = f(1000/T)$ are almost invariant from temperature. For the lower acceptor doping levels, n_{hh} is still weakly temperature-dependent, but its slope differs from zero. For example, $E_a \approx 5.4$ meV was calculated from 60 to 240 K with a coefficient of determination being $R^2 \approx 0.9994$ for sample #3. This energy value corresponds to thermal energy at about 65 K above which the cleavage of the mobility spectra peaks disappears, and the Fermi level is very close to the edge of the valence band. Moreover, it is very interesting that for a degenerate regime ($T < 90$ K), thermal activation energy of sample #2 shows similar value – around 4 meV but with negative sign. After crossing out E_F above the valence band edge, the sign switched to positive and $E_a \approx 28.5$ meV was calculated for temperatures in the range from 100 to 240 K, with $R^2 \approx 0.996$. A final observation related to E_a is that the difference in value between the two energies described above is equal to the

thermal energy at 260 K (≈ 23 meV). For most of the samples at this temperature, $S(\mu)d\mu$ functions showed a slight change compared to adjacent temperature points.

3.3. Heavy-to-light hole effective mass ratio

The $n_{lh}(T)$ and $n_{hh}(T)$ concentration calculations from the previous section, together with (2) allowed to determine the experimental m_{lh}^{dos} -to- m_{hh}^{dos} ratio. The results were presented in Fig. 8.

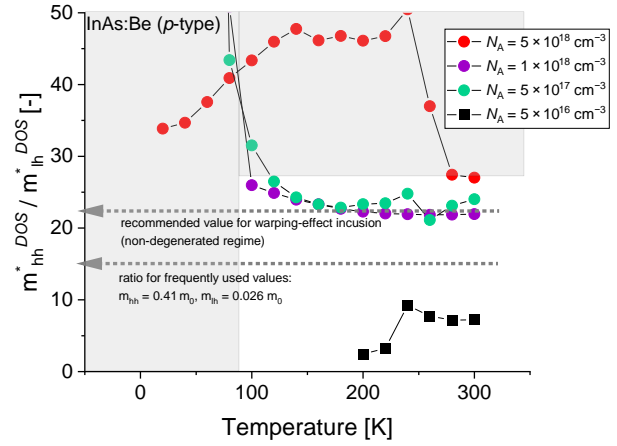


Fig. 8. The set of heavy-to-light hole density-of-state effective mass calculations for the set of InAs:Be samples. The shaded area is interpreted as related to the degenerate regime.

Here, the shaded region has been excluded from the analysis as the one for which the Fermi level is below the top of the valence band. For which the assumptions of (1) are not met. At other points, the ratio of m_{lh}^{dos} -to- m_{hh}^{dos} takes on a value of 22.5 for several samples. It is much higher than 15.8, originated from frequently used values for InAs from a (probably) isotropic and parabolic approximation. Namely, $m_{hh}^{dos} = 0.41 m_0$ and $m_{lh}^{dos} = 0.026 m_0$ are suggested by the Ioffe database [46].

It may be partially justified by a rather complicated valence band structure of InAs which strongly depends on crystal orientation [23]. This specificity of the valence bands in InAs has been discussed in the Nakwaski comprehensive review about A^{III}-B^V binaries [47]. He recommended to take into account a strong anisotropy of m_{hh} and calculate DOS mass in the anisotropic parabolic approximation,

$$m_{eff}^{dos} = (m_1^* m_2^* m_3^*)^{1/3}, \quad (6)$$

where m_1^* , m_2^* , m_3^* are the effective masses along the principal axes of the ellipsoidal energy surface for the considered band. Reference 47 also presented room temperature values for [100] and [111] directions as follows: $m_{hh}^{[100]} = 0.35 m_0$ and $m_{hh}^{[111]} = 0.85 m_0$ and recommended m_{hh}^{dos} in the order of $0.57 m_0$ [see (6)]. However, in this review, he did not focus on m_{lh}^{dos} suggested values and its temperature dependencies.

The additional information can be found in the Vurgaftman and Mayer later review [48] in which they recommended the following Luttinger parameters: $\gamma_1 = 20$,

$\gamma_2 = 8.5$, $\gamma_1 = 9.2$, simultaneously stressing “considerable uncertainty involved in this estimate”. By using the relations collected by Kim *et al.* [24]

$$m_{hh}^* [100] = \frac{1}{\gamma_1 - 2\gamma_2} \quad m_{th}^* [100] = \frac{1}{\gamma_1 + 2\gamma_2} \quad (7a)$$

$$m_{hh}^* [111] = \frac{1}{\gamma_1 - 2\gamma_3} \quad m_{th}^* [111] = \frac{1}{\gamma_1 + 2\gamma_3} \quad (7b)$$

$$m_{hh}^* [110] = \frac{1}{2\gamma_1 - \gamma_2 - 3\gamma_3} \quad m_{th}^* [110] = \frac{1}{2\gamma_1 + \gamma_2 + 3\gamma_3} \quad (7c)$$

values of the m_{th}^* , normalized to m_0 , can be recalculated for the directions of [100], [111], and [110] as follows: $0.027m_0$, $0.026m_0$, $0.013m_0$ which gives $m_{th}^{dos} = 0.021m_0$. Simultaneously, the corresponding values for the heavy-holes band for the directions of [100], [111], and [110] are: $0.333m_0$, $0.625m_0$, $0.256m_0$, which gives $m_{hh}^{dos} = 0.38m_0$ – much closer to the isotropic approximation, but much lower than $0.57m_0$ suggested by Nakwaski. Based on their suggestions, the ratio m_{th}^{dos} -to- m_{hh}^{dos} should be around 18.

The problem of estimating the InAs DOS effective masses has been recently considered by Mecholsky, Resca, and others [44, 45]. They departed from the anisotropic parabolic approximation and performed more detailed calculations as a function of the selected angles. The “band warping” effect inclusion gave them finally $m_{th}^{dos} = 0.0267m_0$ and $m_{hh}^{dos} = 0.6m_0$ which results in the m_{th}^{dos} -to- m_{hh}^{dos} ratio around 22.47.

The above theoretical value of heavy-to-light hole effective mass ratio agrees very well with the magneto-transport measurements and the MSA analysis presented in this work. The authors’ results are summarised in Fig. 8, from which the authors infer the recommended value of this important parameter as 22.5. It is valid for a range of values $N_A = 0.1\text{--}1.0 \cdot 10^{18} \text{ cm}^{-3}$ and $T > 80 \text{ K}$. For higher N_A and lower T , the degenerate statistics should be considered. Moreover, for acceptor concentrations below $1.0 \cdot 10^{17} \text{ cm}^{-3}$, the valence band parabolic approximations seem to be a sufficient computational compromise.

The presented results should be useful not only for the purposes of numerical modelling of microelectronic structures in which the effective masses are one of the key parameters in determining the effective DOS. It is also crucial in the further stage, namely obtaining the self-consistent potential profile of a structure. Its precise determination has a major impact on the self-consistent solution of the Schrödinger-Poisson equations of nanometer-thick layers [49, 50] and, as a result, a precise bandgap engineering [51]. Some of these structures are currently playing an important role in infrared detection, e.g., Ga-free InAs/InAsSb superlattices [52].

4. Conclusions

The work includes the comprehensive magneto-transport studies for a series of InAs samples with beryllium p-type doping every half order of magnitude. The detailed analysis of the mobility spectra in a wide temperature range allowed for conclusions about the applicability range of various models of the valence band geometry, concluding that for

a typical p-type layer with $N_A = 0.1\text{--}1.0 \cdot 10^{18} \text{ cm}^{-3}$ and temperatures above 80 K, valence band effective masses with warping effect inclusion are currently the best approximation. For higher $N_A > 1.0 \cdot 10^{18} \text{ cm}^{-3}$ doping values, it is necessary to take into account degenerate statistics and carefully selected models for the hole mobility description. As it was shown, in degenerate regime, temperature trends of mobility for heavy- and light-holes are uncorrelated.

Authors’ statement by CRediT taxonomy

Conceptualization: Ja.W.; Methodology: Ja.W., G.A.U.M.; Writing – original draft: Ja.W., S.Z.; Resources: J.B., A.K.; Formal analysis: Ja.W., Je.W.; Investigation: Ja.W., G.A.U.M., P.M.; Data curation: S.Z., Ja.W.; Visualization: Ja.W.; Project administration: Ja.W.; Funding acquisition: Ja.W.; Writing – review & editing: J.A., L.F., Je.W.

Acknowledgements

This work has been completed with the financial support of the Ministry of Education and Science (MEiN) under the program “Regional Initiative of Excellence” in 2019–2023; project no. 014/RID/2018/19. funding amount of 4 589 200.00 PLN. Additionally, G.A.U.M., J. A., and L. F contribution to this work was supported by the Australian Research Council (DP200103648).

References

- [1] Kroemer, H. The 6.1Å family (InAs, GaSb, AlSb) and its heterostructures: a selective review. *Physica E* **20**, 196–203 (2004). <https://doi.org/10.1016/j.physe.2003.08.003>
- [2] Webster, P. T. *et al.* Measurement of InAsSb bandgap energy and InAs/InAsSb band edge positions using spectroscopic ellipsometry and photoluminescence spectroscopy. *J. Appl. Phys.* **118**, 245706 (2015). <https://doi.org/10.1063/1.4939293>
- [3] Mueller, S. *et al.* Edge transport in InAs and InAs/GaSb quantum wells. *Phys. Rev. B* **96**, 075406 (2017). <https://doi.org/10.1103/PhysRevB.96.075406>
- [4] Wrobel, J. *et al.* Analysis of temperature dependence of dark current mechanisms in mid-wavelength infrared pin type-II superlattice photodiodes. *Sens. Mater* **26**, 235–244 (2014). https://sensors.myu-group.co.jp/sm_pdf/SM987.pdf
- [5] Bryllert, T., Wernersson, L., Froberg, L. E. & Samuelson, L. Vertical high-mobility wrap-gated InAs nanowire transistor. *IEEE Electron Device Lett.* **27**, 323–325 (2006). <https://doi.org/10.1109/LED.2006.873371>
- [6] Tschirky, T. *et al.* Scattering mechanisms of highest-mobility InAs/AlGaSb quantum wells. *Phys. Rev. B* **95**, 115304 (2017). <https://doi.org/10.1103/PhysRevB.95.115304>
- [7] Rogalski, A. *Infrared and Terahertz Detectors. Third Edition* (CRC Press, 2019).
- [8] Kang, S. S. *et al.* InAs on GaAs photodetectors using thin InAlAs graded buffers and their application to exceeding short-wave infrared imaging at 300 K. *Sci. Rep.* **9**, 12875 (2019). <https://doi.org/10.1038/s41598-019-49300-z>
- [9] Pan, D. *et al.* Dimension engineering of high-quality InAs nanostructures on a wafer scale. *Nano Lett.* **19**, 1632–1642 (2019). <https://doi.org/10.1021/acs.nanolett.8b04561>
- [10] Pidgeon, C. R., Mitchell, D. L. & Brown, R. N. Interband magnetoabsorption in InAs and InSb. *Phys. Rev.* **154**, 737–742 (1967). <https://doi.org/10.1103/PhysRev.154.737>
- [11] Adachi, E. Energy band parameters of InAs at various temperatures. *J. Phys. Soc. Japan* **24**, 1178–1178 (1968). <https://doi.org/10.1143/JPSJ.24.1178>

- [12] Matossi, F. & Stern, F. Temperature dependence of optical absorption in p-type indium arsenide. *Phys. Rev.* **111**, 472–475 (1958). <https://doi.org/10.1103/PhysRev.111.472>
- [13] Braunstein, R. & Kane, E. O. The valence band structure of the III–V compounds. *J. Phys. Chem. Solids* **23**, 1423–1431 (1962). [https://doi.org/10.1016/0022-3697\(62\)90195-6](https://doi.org/10.1016/0022-3697(62)90195-6)
- [14] Kranzer, D. Mobility of holes of zinc-blende III–V and II–VI compounds. *Phys. Status Solidi A* **26**, 11–52 (1974). <https://doi.org/10.1002/pssa.2210260102>
- [15] Hrivnák, L. New relations for band-edge offsets in lattice matched heterojunctions. *Acta Phys. Slovaca* **38**, 346–357 (1988).
- [16] Fischetti, M. V. & Higman, J. M. Theory and Calculation Of The Deformation Potential Electron-Phonon Scattering Rates in Semiconductors. in *Monte Carlo Device Simulation: Full Band and Beyond* (ed. Hess K.) 123–160 (Springer, US, 1991).
- [17] Krijn, M. P. C. M. Heterojunction band offsets and effective masses in III–V quaternary alloys. *Semicond. Sci. Technol.* **6**, 27–31 (1991). <https://doi.org/10.1088/0268-1242/6/1/005>
- [18] Davidovich, M. A. Effects of carrier mass differences on the I–V characteristics of resonant interband tunneling structures in the presence of parallel magnetic field. *J. Appl. Phys.* **78**, 5467–5473 (1995). <https://doi.org/10.1063/1.359662>
- [19] Mikhailova, M. P. Indium Arsenide (InAs). in *Handbook Series on Semiconductor Parameters* (eds. Levinstein, M., Rumyantsev, S. & Shur, M.) Ch. 7, 147–168 (World Scientific, 1996).
- [20] Boykin, T. B., Klimeck, G., Bowen, R. C. & Lake, R. Effective-mass reproducibility of the nearest-neighbor sp^3s^* models: Analytic results. *Phys. Rev. B* **56**, 4102–4107 (1997). <https://doi.org/10.1103/PhysRevB.56.4102>
- [21] Vurgaftman, I., Meyer, J. R. & Ram-Mohan, L. R. Band parameters for III–V compound semiconductors and their alloys. *J. Appl. Phys.* **89**, 5815–5875 (2001). <https://doi.org/10.1063/1.1368156>
- [22] Kim, Y.-S., Hummer, K. & Kresse, G. Accurate band structures and effective masses for InP, InAs, and InSb using hybrid functionals. *Phys. Rev. B* **80**, 035203 (2009). <https://doi.org/10.1103/PhysRevB.80.035203>
- [23] Kim, J. & Fischetti, M. V. Electronic band structure calculations for biaxially strained Si, Ge, and III–V semiconductors. *J. Appl. Phys.* **108**, 013710 (2010). <https://doi.org/10.1063/1.3437655>
- [24] Kim, Y.-S., Marsman, M., Kresse, G., Tran, F. & Blaha, P. Towards efficient band structure and effective mass calculations for III–V direct band-gap semiconductors. *Phys. Rev. B* **82**, 205212 (2010). <https://doi.org/10.1103/PhysRevB.82.205212>
- [25] Çakan, A., Sevik, C. & Bulutay, C. Strained band edge characteristics from hybrid density functional theory and empirical pseudopotentials: GaAs, GaSb, InAs and InSb. *J. Phys. D* **49**, 1–9 (2016). <https://doi.org/10.1088/0022-3727/49/8/085104>
- [26] Apollinari, G., Prestemon, S. & Zlobin, A. V. Progress with high-field superconducting magnets for high-energy colliders. *Annu. Rev. Nucl. Part. Sci.* **65**, 355–377 (2015). <https://doi.org/10.1146/annurev-nucl-102014-022128>
- [27] Beck, W. A. & Anderson, J. R. Determination of electrical transport properties using a novel magnetic field-dependent Hall technique. *J. Appl. Phys.* **62**, 541–554 (1987). <https://doi.org/10.1063/1.339780>
- [28] Wróbel, J., Złotnik, S., Boguski, J., Kojdecki, M. & Wróbel, J. Charakteryzacja wielokanałowego transportu nośników ładunku dla epitaksjalnych struktur półprzewodnikowych. *Przeł d Elektro-techniczny* **98**, 228–230 (2022). <https://doi.org/10.15199/48.2022.09.53> (in Polish)
- [29] Benyahia, D. et al. Molecular beam epitaxial growth and characterization of InAs layers on GaAs (001) substrate. *Opt. Quantum Electron.* **48**, 428 (2016). <https://doi.org/10.1007/s11082-016-0698-4>
- [30] Kowalewski, A., Martyniuk, P., Markowska, O., Benyahia, D. & Gawron, W. New wet etching solution molar ratio for processing T2SLs InAs/GaSb nBn MWIR infrared detectors grown on GaSb substrates. *Mater. Sci. Semicond. Process.* **41**, 261–264 (2016). <https://doi.org/10.1016/j.mssp.2015.08.034>
- [31] Złotnik, S. et al. Facile and electrically reliable electroplated gold contacts to p-type InAsSb bulk-like epilayers. *Sensors* **21**, 5272 (2021). <https://doi.org/10.3390/s21165272>
- [32] Kowalewski, A., Wróbel, J., Boguski, J., Gorczyca, K. & Martyniuk, P. Semiconductor contact layer characterization in the context of Hall-effect measurements. *Metrol Meas Syst.* **26**, 109–114 (2019). <https://doi.org/10.24425/mms.2019.126324>
- [33] Kala, H. et al. Heavy and light hole transport in nominally undoped GaSb substrates. *Appl. Phys. Lett.* **106**, 032103 (2015). <https://doi.org/10.1063/1.4906489>
- [34] Antoszewski, J., Seymour, D. J., Faraone, L., Meyer, J. R. & Hoffman, C. A. Magneto-transport characterization using quantitative mobility-spectrum analysis. *J. Electron. Mater.* **24**, 1255–1262 (1995). <https://doi.org/10.1007/bf02653082>
- [35] Rothman, J., Meilhan, J., Perrais, G., Belle, J. P. & Gravrand, O. Maximum entropy mobility spectrum analysis of HgCdTe heterostructures. *J. Electron. Mater.* **35**, 1174–1184 (2006). <https://doi.org/10.1007/s11664-006-0238-2>
- [36] Antoszewski, J., Umana-Membreno, G. A. & Faraone, L. High-resolution mobility spectrum analysis of multicarrier transport in advanced infrared materials. *J. Electron. Mater.* **41**, 2816–2823 (2012). <https://doi.org/10.1007/s11664-012-1978-9>
- [37] Piper, L. F. J., Veal, T. D., Lowe, M. J. & McConville, C. F. Electron depletion at InAs free surfaces: Doping-induced acceptorlike gap states. *Phys. Rev. B* **73**, 195321 (2006). <https://doi.org/10.1103/PhysRevB.73.195321>
- [38] Olsson, L. Ö. et al. Charge accumulation at InAs surfaces. *Phys. Rev. Lett.* **76**, 3626–3629 (1996). <https://doi.org/10.1103/PhysRevLett.76.3626>
- [39] Wrobel, J. et al. Locally-strain-induced heavy-hole-band splitting observed in mobility spectrum of p-type InAs grown on GaAs. *Phys. Status Solidi-Rapid Res. Lett.* **14**, 1900604 (2020). <https://doi.org/10.1002/pssr.201900604>
- [40] Yao, Y., Bo, B. & Liu, C. The hopping variable range conduction in amorphous InAs thin films. *Curr. Appl. Phys.* **18**, 1492–1495 (2018). <https://doi.org/10.1016/j.cap.2018.09.005>
- [41] Śnieżek, D. et al. Quantum transport and mobility spectrum of topological carriers in (001) SnTe/PbTe heterojunctions. *Phys. Rev. B* **107**, 045103 (2023). <https://doi.org/10.1103/PhysRevB.107.045103>
- [42] Diakite, Y. I., Malozovsky, Y., Bamba, C. O., Franklin, L. & Bagayoko, D. First principle calculation of accurate electronic and related properties of zinc blende indium arsenide (zb-InAs). *Materials* **15**, 3690 (2022). <https://doi.org/10.3390/ma15103690>
- [43] Boykin, T. B., Gamble, L. J., Klimeck, G. & Bowen, R. C. Valence-band warping in tight-binding models. *Phys. Rev. B* **59**, 7301–7304 (1999). <https://doi.org/10.1103/PhysRevB.59.7301>
- [44] Mecholsky, N. A., Resca, L., Pegg, I. L. & Fornari, M. Theory of band warping and its effects on thermoelectronic transport properties. *Phys. Rev. B* **89**, 155131 (2014). <https://doi.org/10.1103/PhysRevB.89.155131>
- [45] Resca, L., Mecholsky, N. A. & Pegg, I. L. Band warping, band non-parabolicity, and Dirac points in electronic and lattice structures. *Physica B Condens. Matter.* **522**, 66–74 (2017). <https://doi.org/10.1016/j.physb.2017.07.046>
- [46] *Ioffe database (InAs)*, <http://www.ioffe.ru/SVA/NSM/Semicond/InAs/bandstr.html#Masses> (1990).
- [47] Nakwaski, W. Effective masses of electrons and heavy holes in GaAs, InAs, AlAs and their ternary compounds. *Physica B Condens. Matter* **210**, 1–25 (1995). [https://doi.org/10.1016/0921-4526\(94\)00921-H](https://doi.org/10.1016/0921-4526(94)00921-H)
- [48] Vurgaftman, I., Meyer, J. R. & Ram-Mohan, L. R. Band parameters for III–V compound semiconductors and their alloys. *J. Appl. Phys.* **89**, 5815–5875 (2001). <https://doi.org/10.1063/1.1368156>
- [49] Ram-Mohan, L. R., Yoo, K. H. & Moussa, J. The Schrödinger–Poisson self-consistency in layered quantum semiconductor structures. *J. Appl. Phys.* **95**, 3081–3092 (2004). <https://doi.org/10.1063/1.1649458>
- [50] Lackner, D. et al. InAs/InAsSb strain balanced superlattices for optical detectors: Material properties and energy band simulations. *J. Appl. Phys.* **111**, 034507 (2012). <https://doi.org/10.1063/1.3681328>
- [51] Kopytko, M. et al. Engineering the bandgap of unipolar HgCdTe-based nBn infrared photodetectors. *J. Electron. Mater.* **44**, 158–166 (2015). <https://doi.org/10.1007/s11664-014-3511-9>
- [52] Ting, D. Z. et al. Long and very long wavelength InAs/InAsSb superlattice complementary barrier infrared detectors. *J. Electron. Mater.* **51**, 4666–4674 (2022). <https://doi.org/10.1007/s11664-022-09561-3>